Journal of Alloys and Compounds 698 (2017) 957–966

Contents lists available at ScienceDirect

Journal of Alloys and Compounds

journal homepage: http://www.elsevier.com/locate/jalcom

Deformation structures and strengthening mechanisms in an Al–Mg–Sc–Zr alloy

S. Malopheyev*, V. Kulitskiy, R. Kaibyshev

Belgorod State University, Pobeda 85, Belgorod 308015, Russia

ARTICLE INFO

Article history:
Received 29 September 2016
Received in revised form
21 December 2016
Accepted 22 December 2016
Available online 24 December 2016

Keywords:
Aluminum alloys
Equal-channel angular pressing
Grain refinement
Mechanical characterization
Grain boundaries
Strengthening mechanisms

ABSTRACT

The deformation structures, mechanical properties and strengthening mechanisms of an Al-5.4 Mg-0.4 Mn-0.2Sc-0.09Zr alloy subjected to equal-channel angular pressing (ECAP) for 12 passes at 573 K (300 °C) were studied. The yield stress (YS) increased gradually with increasing strain from 245 to 350 MPa, and the ultimate tensile strength (UTS) was nearly independent of the strain. An analysis of the strengthening mechanisms indicated that the increase in YS with the number of ECAP passes was attributable to increased contributions from dislocation and boundary strengthening. A "composite" Hall-Petch relationship, $\sigma_{0.2} = 155 + \alpha MGb\rho^{1/2} + 0.11 \times d_{GB}^{-1/2}$, where d_{GB} is the distance between boundaries with misorientations of >2°, ρ is the dislocation forest density, α is a constant, M is the Taylor factor, b is the Burger's vector, and G is the shear modulus, describes the effect of ECAP on the YS with a satisfactory accuracy. No change in the dispersion of the secondary phases during ECAP was observed; therefore, contributions from dispersion strengthening and solid solution strengthening to the overall YS were independent of the strain.

1. Introduction

Non-age-hardenable Al–Mg alloys are widely used due to their good weldability, ductility, toughness, formability and high levels of corrosion resistance [1]. However, these alloys, in their annealed condition, exhibit low yield stresses (YSs), ranging from 90 to 160 MPa, depending on the Mg content [1,2]. A magnesium concentration reaching approximately 5 wt% in aluminum alloys has been found to remain in the solid solution and has effectively increased the strength [1,3,4]. Minor additions of Sc and Zr to an Al–Mg solution lead to the formation of well-distributed, nanoscale coherent $Al_3(Sc,Zr)$ precipitates, which are thermodynamically stable. These particles are highly effective in pinning dislocations and grain boundaries, thus imparting significant strengthening and promoting microstructure stabilization [5,6]. The strengthening mechanism of $Al_3(Sc,Zr)$ precipitates depends on their size [5]. At dispersoid sizes less than ~25 nm, the mechanism of particle shearing dominates the particle bowing mechanism [5].

The superior properties of the Al–Mg materials could be further improved via the formation of an ultrafine-grained (UFG) microstructure. Severe plastic deformation (SPD) is one of the most effective approaches for this purpose [7–11]. Among the various SPD methods, equal-channel angular pressing (ECAP) appears to be particularly attractive due to its relative simplicity and ability to produce UFG structures in large-scale billets [7,11–13]. The strength increase via grain refinement can be predicted by the well-known Hall-Petch (HP) relationship [7,9,11,12,14–21]:

$$\sigma_{0.2} = \sigma_o + k_y\, d^{-0.5} \quad (1)$$

where σ_o is the friction stress, k_y is the HP slope, and d is the crystallite size. During ECAP, continuous dynamic recrystallization (CDRX) [11–13,15,22–28] is the primary mechanism that results in grain refinement in aluminum alloys subjected to ECAP over a temperature interval from 250 to 400 °C. In general, CDRX includes the formation of stable, three-dimensional (3D) arrays of deformation-induced low-angle boundaries (LABs) due to dislocation rearrangement followed by their gradual transformation into high-angle boundaries (HABs) [15,22–27]. The new grains form due to an increase in sub-boundary misorientation resulting from the continuous accumulation of dislocations introduced by the deformation [15,22–28]. Therefore, the average misorientation of the deformation-induced boundaries gradually increases from low to high angles as the strain increases; the deformation structure evolves from a crystallite delimited entirely by LABs to crystallites

* Corresponding author.
E-mail addresses: malofeev@bsu.edu.ru (S. Malopheyev), kulitskiy@bsu.edu.ru (V. Kulitskiy), rustam_kaibyshev@bsu.edu.ru (R. Kaibyshev).

http://dx.doi.org/10.1016/j.jallcom.2016.12.289
0925-8388/

bounded partly by LABs and partly by HABs and, finally, to true UFGs bounded by HABs [23–28].

LABs and HABs hinder dislocation glide; therefore, the number of these obstacles increases with strain that leads to increasing YSs [7,15,17–19,29,30]. The contribution of the newly formed LABs to the overall strength is strongly dependent on their misorientation. Kamikawa et al. [16] established that for pure Al subjected to SPD at room temperature, there is a critical misorientation angle that separates LABs, contributing to dislocation strengthening from boundaries that contribute to grain boundary strengthening. The LABs with misorientations of <3° provide additional strengthening through a dislocation strengthening mechanism [15,16,31]. However, LABs with misorientation angles greater than 3° act as conventional grain boundaries in terms of their strength contribution [16,29,31]. In addition, the lattice dislocation density increases by a factor ≥10 during ECAP [8,15,23–28].

Presently, the contributions from the different strengthening mechanisms to the overall YS for Al–Mg alloys subjected to SPD are not well-understood. R.Z. Valiev et al. assumed that grain boundary strengthening in accordance with the HP law (Eq. (1)) provides the main contribution to the increment of YS due to SPD. Boundary strain-induced segregation of Mg solutes and/or precipitation of Mg-rich clusters near grain boundaries may strongly increase the efficiency of grain boundary strengthening [7,15,32]. From another perspective, dislocation strengthening may be the primary contributor to the overall increase in YS due to SPD in Al–Mg alloys [29]. Examination of the HP law (Eq. (1)) in Al–Mg alloys with a dislocation density $\rho \sim 10^{14}$ m^{-2} without considering the contribution of the dislocation strengthening leads to an overestimation of the k_y value [5,29]. In addition, an increase in the dislocation density by thermomechanical processing [33] may significantly affect the efficiency of grain boundary strengthening in Al–Mg alloys. Therefore, the analysis and consideration of all strengthening mechanisms contributing to the increase in the YS due to grain refinement through ECAP is challenging. The aim of this study was to examine the effect of the deformation structure on the YS of an Al–Mg–Sc–Zr alloy subjected to ECAP at 573 K (300 °C) in terms of the strengthening mechanisms. Specific attention was focused on establishing the role of LABs in strengthening the alloy due to SPD. The origin and nature of the effect on the deformation structure with respect to both ultimate tensile strength (UTS) and ductility will be considered in other studies.

2. Materials and methods

The alloy (i.e., 1570C Al), which had a chemical composition of Al-5.41 Mg-0.37 Mn-0.29Ti-0.2Sc-0.09Zr-0.07Fe-0.04Si (in weight %), was manufactured by direct chill casting followed by homogenization annealing at 633 K (360 °C) for 8 h and extrusion at an initial temperature of 653 K (380 °C) to produce ~75% reduction in the cross-section, which is equal to a true strain of ~1.3 [31]. The samples were machined from the central part of the extruded billet parallel to the extrusion direction into 90-mm-long rods with a square cross-section of 20 × 20 mm^2. These rectangular billets were processed by ECAP via route B_C at a temperature of 573 ± 5 K (300 ± 5 °C) using an isothermal die with a square cross-section of 20 × 20 mm^2. The channel had an L-shaped configuration with an intersection angle of 90°. Deformation through this channel produced a strain of ~1 in each pass [7]. The sample was pressed under a pressure (P) and a constant back pressure ($P_b = 0.2P_{max}$) that was applied using a back plunger in the exit channel [7,27,34]. The level of the back pressure was constrained by a computer-controlled hydraulic system. The rods were pressed up to strains of ~1, ~2, ~4, ~6, ~8 and ~12 with a pressing speed of ~5 mm/s. The total time that each billet was held at the deformation temperature between each ECAP pass was ~3 min per pressing pass. The total time between the final ECAP pass and water quenching was ~1 min.

The specimens for microstructural examination were cut from the central parts of the pressed rods in a longitudinal direction parallel to the last pressing direction (i.e., the deformation microstructures in the longitudinal plane (Y) [7,24] from the central part of the extruded rods were examined) (Fig. 1). The samples for EBSD were electropolished using a standard 25% HNO_3 + 75% CH_3OH solution at 241 K (−32 °C) and 19.5 V to produce a strain-free surface [26]. The EBSD analysis was performed using an FEI Quanta 600FEG SEM equipped with a high-resolution electron backscatter analyzer [26,27]. HABs and LABs were defined when adjacent pixels in the map exhibited a misorientation of >15° and 2°<$\theta \leq$ 15° and are depicted in the misorientation maps using black and white lines, respectively [23,26,27]. The scanning step size was 0.2 μm. The Taylor factor (M) was derived from the EBSD data considering the deformation direction during the tensile tests to measure the mechanical characteristics. The samples for the transmission electron microscopy (TEM) investigation were mechanically thinned and electropolished using the standard 25% HNO_3 + 75% CH_3OH solution at 241 K (−32 °C) and 19.5 V and a Tenupol-5 twinjet polishing unit. The study was performed using a JEM-2100EX TEM operating at 200 kV and equipped with an EDAX energy dispersive X-ray analyzer. The dislocation density was estimated by counting the individual dislocations crossing the thin foil surface [23,35]. The misorientations on the LABs with misorientations of $\theta \leq 2°$ were additionally studied using a conventional Kikuchi-line technique [26,35].

Room-temperature tensile tests to failure were conducted at a constant crosshead velocity corresponding to an initial strain rate of 10^{-3} s^{-1} using an Instron 5882 universal testing machine. Tensile samples with a 35-mm-gauge length and a 7 × 3-mm^2 cross-sectional area were cut along the last pressing direction. The surfaces of all of the tensile specimens were mechanically polished.

3. Results

3.1. Initial structure

The typical deformation structure in the initial condition is shown in Fig. 2. The relevant material microstructural characteristics are summarized in Table 1. The average dimensions of the initial grains in the extrusion direction and normal directions were

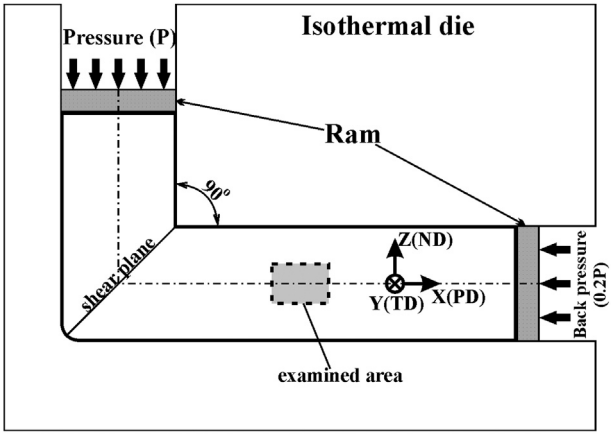

Fig. 1. Schematic illustration of ECAP with three defined X, Y and Z orthogonal planes in the sample. PD, ND and TD are the pressing, normal and transversal directions, respectively. The gray rectangle shows the area for the EBSD analysis and the TEM observations presented in Figs. 3 and 4, respectively (see Section 2 for details).

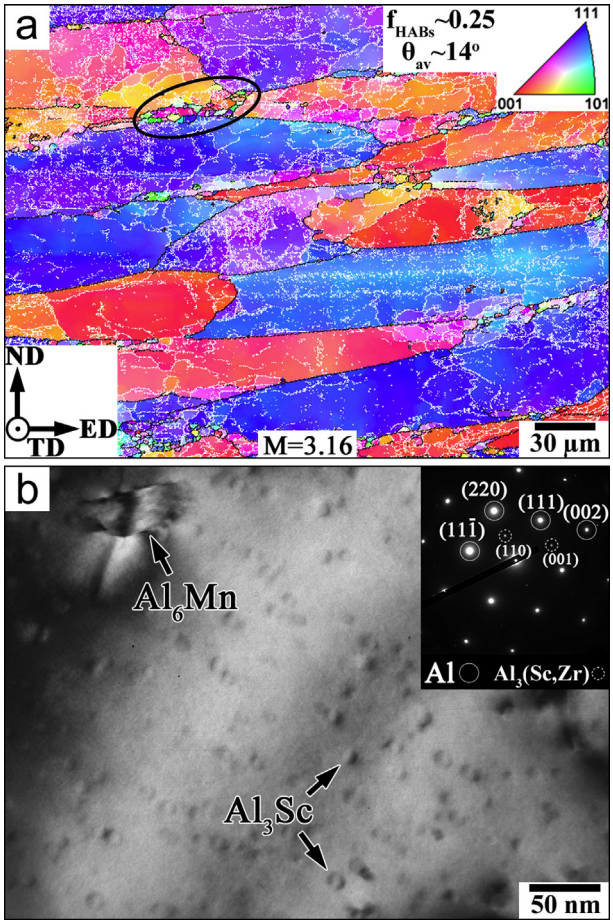

Fig. 2. Initial microstructure after hot extrusion: (a) EBSD map and (b) TEM micrograph. In (b), the diffraction pattern in the top right corner illustrates the coherent nature of the $Al_3(Sc,Zr)$ precipitates. The values of f_{HABs}, θ_{av}, and M indicate the HAB fraction, the average misorientation of the boundaries and the Taylor factor, respectively. ED, ND and TD are the extrusion, normal and transversal directions, respectively. The selected area in (a) shows the recrystallized grains (see Section 3.1 for details).

~93 and ~30 μm (Fig. 2a), respectively. Relatively coarse (sub)grains delimited by the LABs with misorientations typically ranging from 2 to 4° were observed. The average distance between the boundaries with misorientation ≥2° was measured as ~5.5 μm (Table 1). The fraction of the HABs was ~0.25, and the average misorientation was 14° (Fig. 2a). The volume of the recrystallized grains with average dimensions in the longitudinal and normal directions of ~7.6 and ~2.7 μm, respectively, was negligible (i.e.,~0.02) (selected area in Fig. 2a). These grains were observed along the initial boundaries. The density of the lattice dislocations was low (Table 1). The Taylor factor was 3.16 (Fig. 2a).

Two types of nanoscale dispersoids were observed. Coherent $Al_3(Sc,Zr)$ dispersoids with a size of ~10 nm were uniformly distributed, and round Al_6Mn-phase particles with an average size of ~40 nm were occasionally observed within the grains (Fig. 2b). The coffee-bean contrast and orientation relationship (see the diffraction pattern in the top right corner of Fig. 2b) confirm the coherent nature of the $Al_3(Sc,Zr)$ dispersoids. It is important to note that the Al_6Mn particles were easily distinguishable by the size and the origin of the interface boundaries (Fig. 2b). Additional details for this microstructure have been previously described [31].

3.2. Deformation structure after ECAP

Typical EBSD maps and TEM micrographs of the deformation microstructures are shown in Figs. 3 and 4, respectively. The first ECAP pass led to a slight elongation of the initial grains in the pressing direction and the extensive formation of a band-like net of LABs with an average crystallite size of ~1.5 μm. The misorientations of the longitudinal LABs were higher than those of the transverse LABs (Fig. 4a). The fraction of the HABs and the average misorientation increased to ~0.28 and 13.7°, respectively (Fig. 3a). The dislocation density increased by a factor of 4 (Table 1).

For ε~2, a well-defined (sub)grain structure evolves within the elongated initial grains. The fraction of HABs and the average misorientation became ~30% and ~14.5°, respectively (Fig. 3b). The size of the (sub)grains decreased to ~0.95 μm (Fig. 4b). Most of the crystallites distinguished by TEM (Fig. 4b) were round. Planar HABs with an inclination angle of ~26° to the pressing direction were observed (selected areas in Fig. 3b). The density of the lattice dislocations within the (sub)grains increased by a factor of 10 compared to the initial material condition and decreased insignificantly upon further strain (Table 1).

For ε~4, a partially recrystallized structure was observed (Fig. 3c). Extended planar boundaries evolved within the initial grains with certain orientations (Fig. 3c). Concurrently, bands of recrystallized grains evolved on the original boundaries, and well-defined 3D networks of LABs appeared within the unrecrystallized grains with other orientations (Fig. 3c). The misorientations of the longitudinal and transverse LABs became essentially the same (Fig. 4d), and the deformation-induced crystallites acquired a nearly round shape. The HAB fraction and the average misorientation increased to ~48% and ~21.3°, respectively (Fig. 3c).

With an additional increase in strain, the growth of the recrystallized fraction due to the formation of new layers of recrystallized grains was the primary process responsible for microstructural evolution (Fig. 3d–f). For ε~6, a partially recrystallized structure remained (Fig. 3d). The fraction of recrystallized grains increased insignificantly (Fig. 3d). Concurrently, the HAB fraction and the average misorientation increased slightly (Fig. 3d). The formation of new recrystallized layers occurred simultaneously with the increase in the misorientation of the LABs, which delimited the deformation bands within the unrecrystallized region. For ε~8, a fully recrystallized structure was observed, and the HAB fraction

Table 1
Microstructural characteristics of the 1570C alloy.

Material condition	Boundary distance (μm)[a]	Dislocation density (m^{-2})	Mean diameter of $Al_3(Sc,Zr)$ particles (nm)	Volume fraction of $Al_3(Sc,Zr)$ particles (%)
Initial	5.5	1×10^{13}	4.5	0.1
ECAP 1 pass	1.5	4×10^{13}	4.5	0.1
ECAP 2 passes	1.95	1×10^{14}	4.5	0.1
ECAP 4 passes	0.75	7×10^{13}	4.5	0.1
ECAP 6 passes	0.5	9.5×10^{13}	4.5	0.1
ECAP 8 passes	0.51	6×10^{13}	4.5	0.1
ECAP 12 passes	0.55	5×10^{13}	4.5	0.1

[a] The distance between LABs with misorientation ≥2°.

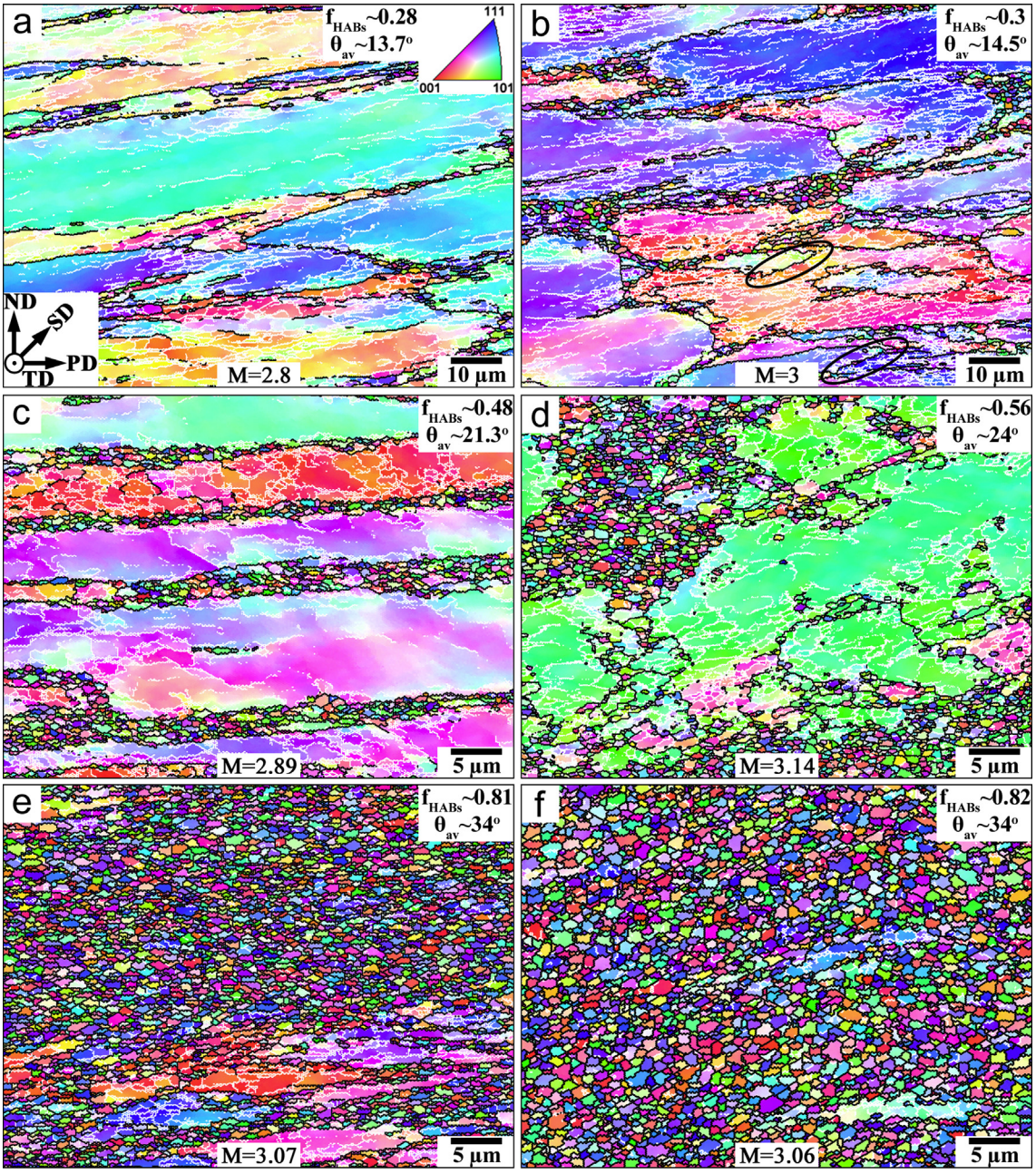

Fig. 3. Typical EBSD maps of ECAPed 1570C Al at: (a) ε~1, (b) ε~2, (c) ε~4, (d) ε~6, (e) ε~8, and (f) ε~12. PD, ND, TD and SD are the pressing, normal, transversal and shear directions, respectively. The values of f_{HABs}, θ_{av}, and M indicate the HAB fraction, the average misorientation and the Taylor factor, respectively. The selected areas in (b) show the alignment of planar HABs along the shear direction [6] (see Section 3.2 for details).

and the average misorientation were ~0.81 and ~34°, respectively (Fig. 3e). At ε~12, the deformation microstructure was the same, and the HAB fraction and the average misorientation remained the same (Fig. 3f). The grains contained a moderate density of lattice dislocations (ρ~5 × 10^{13} m^{-2}). No changes in the average sizes of the Al_3(Sc,Zr) and the Al_6Mn particles were observed.

No boundary segregations of Mg-atoms or the formation of Mg-rich clusters near the HABs were found under any material conditions by elemental mapping of Mg (not shown here).

3.3. Mechanical properties

The engineering stress-strain curves for the 1570C alloy are shown in Fig. 5. The experimental results from the tensile tests, including the YS ($\sigma_{0.2}$), the UTS (σ_{UTS}) and the elongation-to-failure (δ) tests, are summarized in Table 2. The shapes of the σ–ε curves, the type of jerky flow, the average amplitude of the serrations and the YS strongly depend on the material condition. An extensive initial strain hardening and an overall parabolic shape of the σ–ε curves prior to necking were observed in the initial material as well as after the 1st and the 2nd ECAP passes. Repeating oscillations with a serrated characteristic were observed and are known as the Portevin-Le Chatelier (PLC) effect. The PLC effect is conventionally attributed to dynamic strain aging (DSA) in aluminum alloys [29,33,36–38]. The highest magnitude of the stress oscillations increased by a factor of ~2 after the first ECAP pass, remained nearly unchanged in the 2–4 strain interval and then tended to increase as the number of passes increased at $\varepsilon \geq 6$ (Table 2). ECAP leads to a

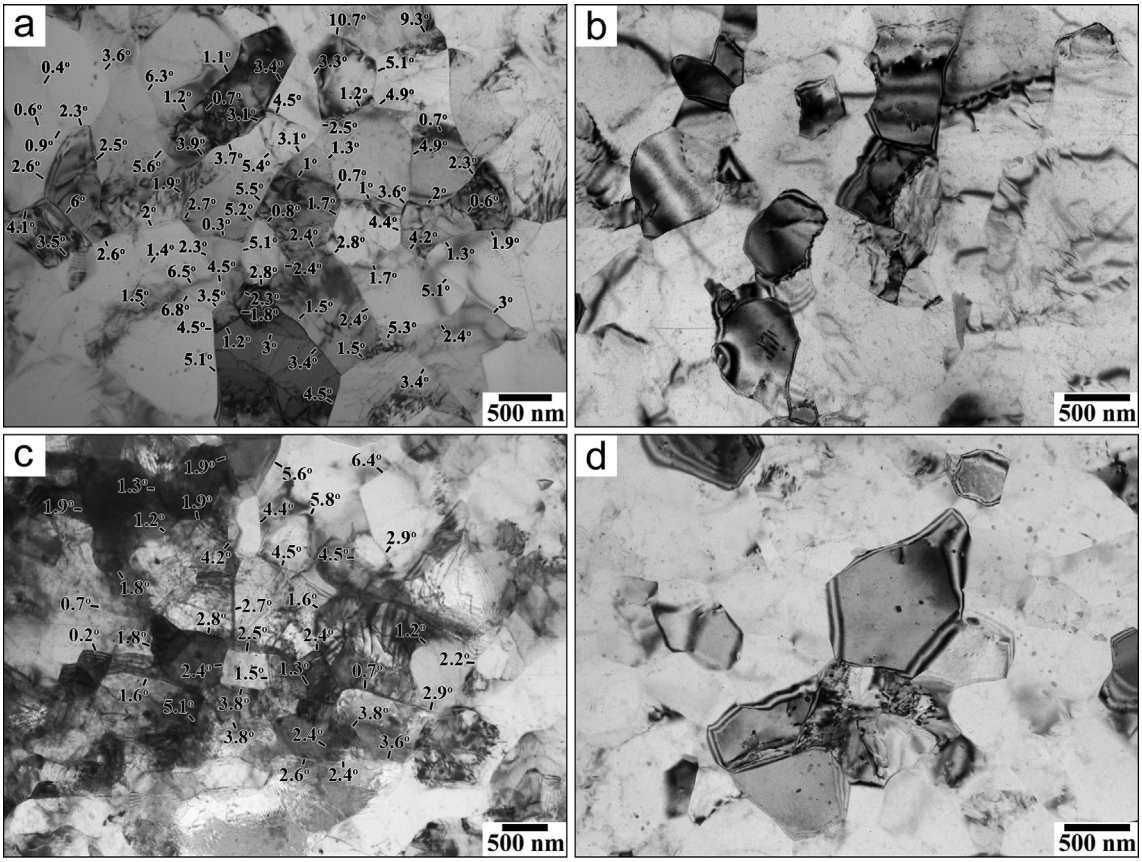

Fig. 4. TEM images of ECAPed 1570C Al at: (a) ε~1, (b) ε~2, (c) ε~4, and (d) ε~8. Misorientations of the LABs are shown in (a) and (c) (see Section 3.2 for details).

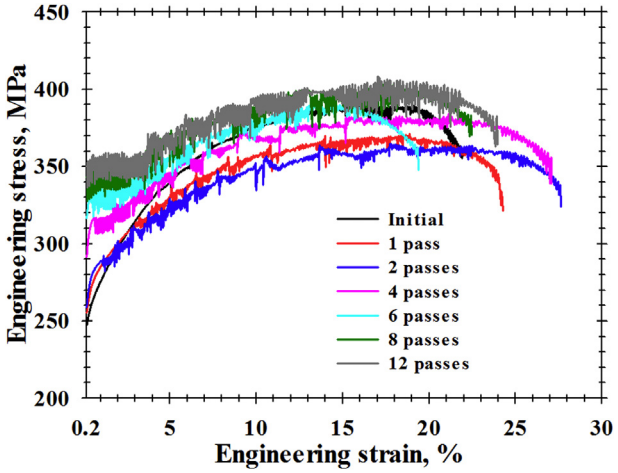

Fig. 5. Typical engineering stress – strain curves of the 1570C alloy subjected to hot extrusion (initial) and ECAP with different numbers of passes.

shift of the onset of jerky flow to low strain and a transition from continuous yielding to discontinuous yielding [39–41]. At $\varepsilon \geq 4$, a plateau was superimposed with the serrations, which can be observed as high-frequency oscillations between the upper and lower yield strengths [38,39,41]. It is important to note that the magnitudes of the stress drops in the 1570C Al alloy are a factor of ~5 higher than those in dilute Al-7 wt.% Mg [42] and Al-5.4 wt% Mg alloys containing a dispersion of incoherent Al_6Mn particles with an average size of 25 nm and a round shape [29].

Work hardening became less pronounced as the number of ECAP passes increased. The overall work-hardening rate represented by the UTS/YS ratio (Table 2) decreased by a factor of ~3.5 after 12 ECAP passes. As a result, the UTS values in the initial material condition, as well as after six or more ECAP passes, were nearly the same. Moreover, ECAP with a low number of passes resulted in a decrease in UTS. Therefore, ECAP provided a +42% increase in the YS after 12 passes and had no positive effect on UTS. The ductility correlated with the UTS values (Table 2) and exhibited no correlation with the work-hardening ability, which is considered crucial for achieving a high elongation-to-failure [4,7,42,43]. The ductility after 12 ECAP passes was even higher than that at the initial material condition, despite strong differences in the work-hardening rate.

4. Discussion

ECAP substantially affects the grain structure and the mechanical properties. The strengthening mechanisms are discussed in this section to elucidate the key issues in the relationship between the deformation structure and the YS. Assuming that different strengthening mechanisms act independently, thus having additive contributions, the overall YS of the 1570C alloy can be expressed as follows:

$$\sigma_{0.2} = \sigma_o^{Al} + \sigma_{SS} + \sigma_p + \sigma_{GB} + \sigma_d \quad (2)$$

where σ_o^{Al} is the resistance to dislocation glide within the grains for the high-purity aluminum, σ_{SS} is the solid solution of the additional elements in the aluminum matrix, σ_p is the dispersion strengthening, σ_d is the dislocation strengthening, and σ_{GB} is the grain

Table 2
Mechanical properties of the 1570C alloy.

Material condition	YS, MPa	UTS, MPa	UTS/YS ratio	Highest the Amplitude Range (MPa) of Stress Oscillations	δ, %
Initial	245	415	1.7	12	23
ECAP 1 pass	250	375	1.5	20	26
ECAP 2 passes	265	380	1.43	18	19.5
ECAP 4 passes	290	380	1.31	18	19
ECAP 6 passes	315	425	1.35	22	18
ECAP 8 passes	345	420	1.22	24	27
ECAP 12 passes	350	420	1.2	26	27.5

boundary strengthening without the σ_o term from Eq. (1). The contributions from these strengthening mechanisms will be analyzed separately.

High-purity aluminum has a low friction stress (σ_o^{Al}) of ~10 MPa [5,16,44,45].

Solid solution strengthening is controlled by the magnesium solute content, which can be expressed as follows [3,46]:

$$\sigma_{SS} = HC^n \tag{3}$$

where C is the concentration of an element in solid solution and n and H are constants [45,46].

In Al–Mg alloys, the YS dependence on the Mg content is not linear [4,5]. Since no detectable β–phase Mg_5Al_8 particles with a spherical shape [1] were observed under any material conditions, the entire Mg content (5.4 wt%) that was retained within the solid solution can be considered for the calculation of the σ_{SS} term. In addition, the 1570C alloy contains ~0.37 wt% Mn in the solid solution that was observed by the elemental mapping of Mn (not shown here). Cooling with a high solidification rate followed by low temperature homogenization [26] resulted in the retention of this portion of Mn within the solid solution, and these solutes can also provide solute strengthening [45,47]. Therefore, the increase in the yield strength due to solid solution strengthening can be expressed as follows [45]:

$$\sigma_{SS} = \sigma_{trace} + H_{Mg}C_{Mg}^n + H_{Mn}C_{Mn}^m \tag{4}$$

where σ_{trace} is approximately 24 MPa [45], $H_{Mg} = 13.8$ MPa/(wt% Mg) [3], $n = 1$ for Al–Mg alloys [3,47], C_{Mg} is the concentration of Mg in weight percent, $H_{Mn} = 18.35$ MPa/(wt.% Mn) [45], C_{Mn} is the concentration of Mn in weight percent, and $m = 0.9$ for the Al–Mg alloys [45,47].

In the Al–Mg–Sc–Zr alloys, general strengthening is due to precipitations associated with coherent Al_3(Sc,Zr) particles. Kendig et al. demonstrated that the mechanism of interaction of the dislocations with the particles is dependent on the size of the coherent dispersoids [5]. For Al_3(Sc,Zr) particles, a shearable to non-shearable transition occurs at a dispersoid dimension of ~25 nm, providing the highest dispersion strengthening [5]. With larger particle sizes, the critical stress for Orowan bowing becomes lower than that required to cut these dispersoids by gliding dislocation. At lower particle dimensions, the shearing mechanism is the most likely the mechanism for the interaction between gliding dislocations. Because the Al_3(Sc,Zr) precipitates were typically finer than 25 nm in diameter under any material condition (Table 1), the particle cutting mechanism is considered to be the mechanism responsible for dispersion strengthening.

Dislocation shearing contributes to the YS via coherency strengthening ($\Delta\sigma_{cs}$), modulus mismatch strengthening ($\Delta\sigma_{ms}$), and chemical strengthening due to interfacial strengthening ($\Delta\sigma_{chi}$) and order strengthening ($\Delta\sigma_{os}$) [48–50]. Precipitation strengthening is determined by the ratio between the $\Delta\sigma_{os}$ and $\Delta\sigma_{cs}+\Delta\sigma_{ms}$ values because coherency strengthening and modulus strengthening occur in sequence [51]. It is important to note that when a dislocation cuts a coherent precipitate, two new ledges are formed, which results in chemical strengthening ($\Delta\sigma_{chi}$) in sequence with both aforementioned strengthening mechanisms. However, the magnitude of the $\Delta\sigma_{chi}$ value is negligible and will not be considered for the calculation of the precipitation strengthening. As shown in previous studies [3,5,31,51], $\Delta\sigma_{os} \gg (\Delta\sigma_{cs}+\Delta\sigma_{ms})$ for the Al_3(Sc,Zr) precipitates with dimensions of ~20 nm; therefore, the strengthening effect, is believed to primarily result from the formation of an anti-phase boundary (APB) within the sheared particle. Therefore, we can simplify to $\sigma_p = \Delta\sigma_{os}$, and the order strengthening can be estimated using the following equation [5]:

$$\sigma_p = M\frac{\gamma^{1.5}}{b^2}\left(\frac{rf}{G}\right)^{0.5} \tag{5}$$

where M is the Taylor factor, γ is the energy required to form the APB, b is the Burger's vector (0.286 nm), G is the shear modulus of aluminum (25.4 GPa), r is the radius of the particles being cut (Table 1) and f is the particle volume fraction (Table 1). The mean Taylor factor was derived from the EBSD data assuming uniaxial tension on the PD. This factor varied from 2.8 to 3.16, depending on the conditions (see Figs. 2 and 3). The APB energy is difficult to determine accurately and has been reported to vary from 0.1 to 0.67 J/m^2, depending on the calculation method [5]. In this study, an APB energy of 0.185 J/m^2 was considered to be a reasonable value, as recommended by Kendig et al. [5].

A traditional method of calculation of the HP slope is based on Eq. (1), where σ_o is specified as the friction resistance for dislocation glide within the crystallite with a size d and consists of contributions of friction stress for the pure metal, σ_o^{Al}, solid solution strengthening, σ_{SS}, and precipitate strengthening, σ_p, but not from dislocations [16,18,52]:

$$\sigma_0^{AlMgScZr} = \sigma_o^{Al} + \sigma_{SS} + \sigma_p \tag{6}$$

The $\sigma_0^{AlMgScZr}$ value of ~155 MPa is independent of the grain size; therefore, it is independent of the number of ECAP passes. The strength contribution due to the additional resistance to dislocation motion caused by the presence of grain boundaries is described by a second term in Eq. (1). However, Eq. (1) could not describe the strength–structure relationship in Al and aluminum alloys with a small grain size produced by SPD, since dislocation and grain boundary strengthening are both dependent on the imposed strain (Table 1) [16]. The estimation of the effect of the grain size on the YS in the materials with fcc lattices and high dislocation densities ($\rho \sim 10^{14}$ m^{-2}), without considering the contribution of the deformation strengthening, overestimates the k_y value from Eq. (1) [5,29]. In addition, the LABs with a low misorientation may contribute to dislocation strengthening, and the LABs with a moderate misorientation may contribute to grain boundary strengthening [15–19,29,31,53]. Therefore, HP behavior is not

solely attributed to grain size for materials with a UFG structure produced by SPD. The YS increase >155 MPa with an increasing number of ECAP passes is attributed to the concurrent increased contributions of dislocation and grain boundary strengthening. The following "composite" HP equation based on the linear additive strengthening contributions from dislocations and grain boundaries was proposed [16,17,54]:

$$\sigma_{0.2} = \sigma_0^{AlMgScZr} + \sigma_{GB} + \sigma_d \quad (7)$$

The dislocation strengthening is described as follows [3,16,17,29,31,52]:

$$\sigma_d = \alpha MGb\rho^{1/2} \quad (8)$$

where ρ is the dislocation forest density (Table 1) and α is a constant ($\approx$0.24). In a previous study [29], it was suggested that in an Al–Mg alloy during equal channel angular pressing at 300 °C, LABs with a very low misorientation (<3°) may contribute to dislocation strengthening, as described in the literature [16,45]. Based on this finding, an expanded version of Eq. (8) was written as follows [16,45]:

$$\sigma_d = \alpha MGb(\rho + \rho_{LABs})^{1/2} \quad (9)$$

where ρ_{LABs} is the dislocation density stored in the LABs, which are capable of being penetrated by gliding dislocations and can contribute to strengthening via forest hardening [15–17,29,45]. The ρ_{LABs} values were calculated using the following equation [15–17]:

$$\rho_{LABs} = \frac{3\theta_{LABs}}{bd_{LABs}} \quad (10)$$

where θ_{LABs} denotes the mean misorientation of the aforementioned dislocation boundaries and d_{LABs} denotes the average distance between the LABs with an average misorientation of <2°, which is calculated from the TEM data, as in the previous work [29].

Using Eq. (9) and considering both the forest dislocation density and the density of dislocations stored in the LABs with a misorientation of $\leq$2° led to an extremely high dislocation strengthening and a significant overestimation of the calculated YS above experimental values since the dislocation density accumulated in these LABs is higher by a factor of ~10 than the density of the lattice dislocations after the first pass. Thus, the authors suggest that ordered LABs with a misorientation <2° produced by ECAP at intermediate temperatures is penetrable for gliding dislocations and contributes insignificantly to the dislocation strengthening, in contrast to aluminum and aluminum alloys processed at room temperature. Under warm deformation, the rearrangement of the lattice dislocations composing these LABs leads to their transformation to regular subboundaries [22], which relieves long-range stress fields. TEM observations showing no evidence for long-range stress fields support this conclusion. Gliding dislocations may easily penetrate a subboundary with a distance between intrinsic dislocations of ~30*b*. This distance in the low-angle boundaries was calculated as follows:

$$d_{dis} = b/\theta \quad (11)$$

where b is the Burger's vector (0.286 nm) and θ is a critical angle of 2°. Therefore, these subboundaries play a role as obstacles with short-range stress fields and may contribute to the $\sigma_0^{AlMgScZr}$ value in the HP relationship [54] and have no sense to dislocation and boundary strengthening.

The contribution from grain boundary strengthening to the overall strength can be calculated as follows:

$$\sigma_{GB} = k_y d_{GB}^{-1/2} \quad (12)$$

where d_{GB} is the average spacing between the boundaries with a misorientation above a critical angle of 2°. The d_{GB} parameter was calculated from the EBSD data as the average spacing of the HABs and all of the LABs with misorientations $\geq$2° (Table 1), suggesting that LABs with misorientations above 2° act as conventional HABs in terms of strength contribution [16,29,31]. It should be noted that ECAP up to 1–6 passes led to elongation of the initial coarse grain and the formation of a lamellar structure. In this case, the d_{GB} parameter in Eq. (12) was taken as a double average interboundary spacing, as recommended by Zhang et al. [55]. The HP slope k_y~0.11 MPa × $m^{1/2}$ was calculated from the plot shown in Fig. 6a representing the YS-σ_d *vs* d_{GB} dependence for $\sigma_0^{AlMgScZr}$ = 155 MPa. Here, the effect of dislocation strengthening, which is in fact correlated with the grain size produced by SPD (Table 1), was removed from the experimental YS values to obtain the "true" value of the HP slope [3,16,42,45,54,56–58]. The HP behavior of the 1570C Al is described as follows:

$$\sigma_{0.2} = 155 + \alpha MGb\rho^{1/2} + 0.11 \times d_{GB}^{-1/2} \quad (13)$$

The "true" k_y value derived from Fig. 6 is higher by a factor of 2.5

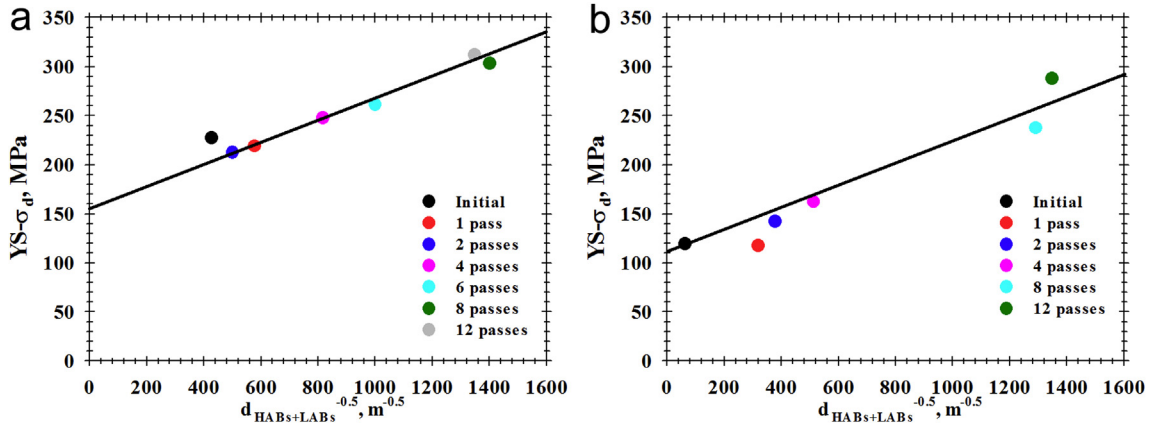

Fig. 6. Experimental yield strength-boundary spacing relationship for the (a) 1570C and (b) Zr-modified AA5083 [22] alloys under the different conditions. The $d_{HABs+LABs}$ parameter is the average spacing of the HABs and all of the LABs with misorientations $\geq$2°. The YS-σ_d parameter is the experimental yield strength excluding dislocation strengthening (see Section 4 for details).

than that reported for pure Al with coarse crystallites outlined by the HABs and the LABs with misorientation >2° [16]. This difference may be attributed to a positive effect of the Mg content on the k_y value [33]. It is obvious that the Mg solutes improve the efficiency of grain boundary strengthening. At the same time, the HP slope for the 1570C alloy is lower than that for steels by a factor of 1.5 [53,55,59] and close to that obtained for a Cu–Cr–Zr bronze [58]. Therefore, the efficiency of the grain boundary strengthening in the present 1570C alloy with a stacking fault energy of ~120 mJ m^{-2} [60] is only slightly lower than that in austenitic steels with a low stacking fault energy [54,56,61] and close to that in other alloys with a fcc lattice and a moderate-to-high value of the stacking fault energy. If the k_y value is calculated for Al–Mg alloys with recrystallized structures containing a nearly similar dislocation density at different grain dimensions, then HP slopes ranging from 0.09 to 0.14 MPa × $m^{1/2}$ were obtained [45,62–64], which are close to the k_y value calculated for the 1570C Al using the "composite" HP relationship (Eq. (7)).

It is worth noting that there is a threefold difference between the apparent k_y value calculated for the original HP relationship and described by Eq. (1) [18,20,21] and the "true" HP slope calculated for a "composite" HP relationship and described by Eq. (7) [16,17,53,54,56] for austenitic steels [54,56]. To evaluate this difference for Al–Mg alloys, the experimental data reported for the Al-5.4%Mg-0.5%Mn-0.1%Zr alloy (in wt.%) [29] were revised through the aforementioned procedure and are presented in Fig. 6b. It is seen that the HP behavior of this Zr-modified AA5083 alloy (AA5083ZrHA1) is described as follows:

$$\sigma_{0.2} = 117 + \alpha M G b \rho^{1/2} + 0.11 \times d_{GB}^{-1/2} \quad (14)$$

Therefore, the precipitation strengthening associated with $Al_3(Sc,Zr)$ dispersoids provides a +32% increase in the friction stress but the "true" k_y value is nearly the same in both Al-5.4%Mg alloys containing coherent and incoherent dispersoids [26,29,31]. There is two-fold difference between the apparent (~0.22 MPa × $m^{1/2}$) [29] and "true" (~0.11 MPa × $m^{1/2}$) k_y values for the Al–Mg alloy subjected to ECAP.

The difference between the experimental and theoretical YS values for the 1570C Al alloy did not exceed 11% (Fig. 7); therefore, the analysis of YS in terms of the additive contributions of the four strengthening mechanisms gives appropriate results. Inspection of Fig. 7 shows that an increase in the YS due to ECAP occurs primarily due to grain boundary strengthening. Dislocation strengthening plays an important but a minor role. Therefore, the superposition of the UFG structure and a high dislocation density is a necessary condition for the fabrication of high-strength products from Al–Mg–Sc–Zr alloys. The use of the "composite" HP law [16,17,53] allowed proper exploration of the origin of the effect of the grain size on YS. The difference in the HP slope ranging from 0.06 to 0.22 MPa × $m^{1/2}$ reported in the literature for Al-Mg [3,5,29,62–65] is associated with the fact that dislocation strengthening can contribute more significantly than can grain boundary strengthening to overall YS, and structures with different grain dimensions were also distinguished by dislocation density. In addition, the LABs with misorientation ≥2 ÷ 3° may play an important role in grain boundary strengthening, as shown above. However, this role is dependent on their origin. Irregular dislocation networks with a misorientation ≤3° contribute significantly to the dislocation strengthening as obstacles inducing long-range stress fields [16], while subboundaries with the same misorientation and inducing short-range stress fields contribute scarcely to the YS.

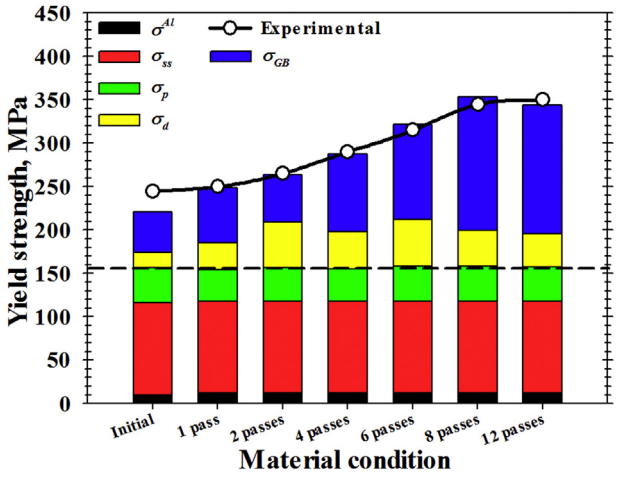

Fig. 7. Comparison between the experimental and calculated yield strengths of the initial and ECAPed 1570C alloy. The horizontal dashed line shows the $\sigma_0^{AlMgScZr}$ value, which is independent of the number of ECAP passes (see Section 4 for details).

It is worth noting that a solid-type solution strengthening mechanism, which is associated with DSA and appears as stress oscillations, can contribute to variable parts of Eq. (1) and Eq. (7). Contribution of the solid solution strengthening from the DSA is considered to be equal to the stress drop size on the stress-strain curves [29,66]:

$$\sigma_{DSA} \approx \sigma_{drop} \quad (15)$$

where σ_{drop} is the maximum drop stress observed on the stress-strain curve (Table 2). It is seen that the highest increment of σ_{DSA} due to ECAP is ~14 MPa, which is essentially the same as the deviations of the experimental datum points from the straight line in Fig. 6. Since the contribution of the solid solution strengthening associated with DSA to the overall YS is comparable in accuracy to the aforementioned analysis for establishment of a "composite" HP relationship for the 1570C alloy, this strengthening mechanism was discarded for simplicity. A good correlation between the experimental and the theoretical YS values (Fig. 7) validated this approach.

Analysis of the aforementioned literature and the present results show that the appropriate k_y value can be calculated with a traditional HP relationship (Eq. (1)) with the stipulation that the variation in grain size is not accompanied by variations in other structural parameters. The use of a "composite" HP relationship as in Eq. (7) provides an appropriate k_y value if the dislocation density varies together with changes in grain dimension stipulating the friction stress, σ_0, involving contributions from the solid solution and particle strengthening that is independent of grain size. For aluminum alloys with ~5.4 wt% Mg and different dispersions of the secondary phase, the k_y value is ~0.11 MPa × $m^{1/2}$. There is ambiguity in the literature data for the effect of Mg solutes on the k_y value in Al alloys.

5. Conclusions

The microstructural evolution and the mechanical properties of the Al-5.4 Mg-0.2Sc-0.09Zr alloy subjected to ECAP were studied. The main conclusions from this study are as follows:

1. At 300 °C, ECAP provided a +140% increase in the yield stress. The ultimate tensile strength remains nearly unchanged, and the elongation-to-failure increased slightly with an increasing number of ECAP passes.
2. The increase in the yield stress was due to dislocation and boundary strengthening. Grain boundary strengthening is the

major contributor to the overall increment of the yield stress due to intensive grain refinement. The strain-induced low-angle boundaries with misorientations >2° contribute to boundary strengthening as high-angle boundaries.

3. The effect of ECAP on yield stress is described by the "composite" Hall-Petch relationship, $\sigma_{0.2} = \sigma_0^{'} + \sigma_{GB} + \sigma_d$, where $\sigma_0^{'}$ is an invariable parameter, which is independent on strain, σ_{GB} and σ_d are variable parameters attributed to grain boundary strengthening and dislocation strengthening, respectively. The σ_{GB} and σ_d parameters are dependent on strain.

Acknowledgments

The financial support received from the Ministry of Education and Science, Russia, (Belgorod State University project №14.587.21.0018 (RFMEFI58715X0018)) is acknowledged. The main results were obtained by using equipment of Joint Research Center, Belgorod State University. The authors would also like to thank Anna Mogucheva for the analysis of the HP relationship and for fruitful discussions.

References

[1] I.J. Polmear, Light Alloys: from Traditional Alloys to Nanocrystals, fourth ed., Butterworth-Heinemann/Elsevier, UK, 2006.
[2] E.A. Brandes, G.B. Brook (Eds.), Smithells Light Metals Handbook, Butterworth-Heinemann, 1998.
[3] T.J. Harrell, T.D. Topping, H. Wen, T. Hu, J.M. Schoenung, E.J. Lavernia, Microstructure and strengthening mechanisms in an ultrafine grained Al-Mg-Sc alloy produced by powder metallurgy, Metall. Mater. Trans. A 45 (2014) 6329–6343.
[4] M. Jobba, R.K. Mishra, M. Niewczas, Flow stress and work-hardening behaviour of Al–Mg binary alloys, Int. J. Plast. 65 (2015) 43–60.
[5] K.L. Kendig, D.B. Miracle, Strengthening mechanisms of an Al-Mg-Sc-Zr alloy, Acta Mater. 50 (2002) 4165–4175.
[6] Y. Deng, Zh Yin, Q. Pan, G. Xu, Y. Duan, Y. Wang, Nano-structure evolution of secondary $Al_3(Sc_{1-x}Zr_x)$ particles during superplastic deformation and their effects on deformation mechanism in Al-Zn-Mg alloys, J. Alloys Compd. 695 (2016) 142–153.
[7] R.Z. Valiev, T.G. Langdon, Principles of equal-channel angular pressing as a processing tool for grain refinement, Prog. Mater. Sci. 51 (2006) 881–981.
[8] O. Sitdikov, T. Sakai, E. Avtokratova, R. Kaibyshev, K. Tsuzaki, Y. Watanabe, Microstructure behavior of Al–Mg–Sc alloy processed by ECAP at elevated temperature, Acta Mater. 56 (2008) 821–834.
[9] H.-J. Lee, J.-K. Han, S. Janakiraman, B. Ahn, M. Kawasaki, T.G. Langdon, Significance of grain refinement on microstructure and mechanical properties of an Al-3% Mg alloy processed by high-pressure torsion, J. Alloys Compd. 686 (2016) 998–1007.
[10] P. Bazarnik, B. Romelczyk, Y. Huang, M. Lewandowska, T.G. Langdon, Effect of applied pressure on microstructure development and homogeneity in an aluminium alloy processed by high-pressure torsion, J. Alloys Compd. 688 (2016) 736–745.
[11] E. Avtokratova, O. Sitdikov, O. Mukhametdinova, M. Markushev, S.V.S.N. Murty, M.J.N.V. Prasad, B.P. Kashyap, Microstructural evolution in Al-Mg-Sc-Zr alloy during severe plastic deformation and annealing, J. Alloys Compd. 673 (2016) 182–194.
[12] H. Jiaa, R. Bjørgeb, K. Marthinsena, Y. Li, The deformation and work hardening behaviour of a SPD processed Al-5Cu alloy, J. Alloys Compd. 697 (2017) 239–248.
[13] Y. Duan, L. Tang, G. Xu, Y. Deng, Z. Yin, Microstructure and mechanical properties of 7005 aluminum alloy processed by room temperature ECAP and subsequent annealing, J. Alloys Compd. 664 (2016) 518–529.
[14] L. Kurmanaeva, T.D. Topping, H. Wen, H. Sugahara, H. Yang, D. Zhang, J.M. Schoenung, E.J. Lavernia, Strengthening mechanisms and deformation behavior of cryomilled Al-Cu-Mg-Ag alloy, J. Alloys Compd. 632 (2016) 591–603.
[15] I. Sabirov, M.Yu Murashkin, R.Z. Valiev, Nanostructured aluminium alloys produced by severe plastic deformation: new horizons in development, Mater. Sci. Eng. A 560 (2013) 1–24.
[16] N. Kamikawa, X. Huang, N. Tsuji, N. Hansen, Strengthening mechanisms in nanostructured high-purity aluminium deformed to high strain and annealed, Acta Mater. 57 (2009) 4198–4208.
[17] A.A. Gazder, W. Cao, ChH.J. Davies, E.V. Pereloma, An EBSD investigation of interstitial-free steel subjected to equal channel angular extrusion, Mater. Sci. Eng. A 497 (2008) 341–352.
[18] M. Kato, Hall-Petch relationship and dislocation model for deformation of ultrafine-grained and nanocrystalline metals, Mater. Trans. 55 (2014) 19–24.
[19] Y. Estrin, A. Vinogradov, Extreme grain refinement by severe plastic deformation: a wealth of challenging science,, Acta Mater. 61 (2013) 782–817.
[20] E.O. Hall, The deformation and ageing of mild steel: III discussion of results, Proc. Roy. Soc. B 64 (1951) 747–753.
[21] N.J. Petch, The cleavage strength of polycrystals, J. Iron Steel Inst. 174 (1953) 25–28.
[22] F.J. Humphreys, M. Hatherly, Recrystallization and Related Annealing Phenomena, Elsevier, Oxford, 2005.
[23] R. Kaibyshev, K. Shipilova, F. Musin, Y. Motohashi, Continuous dynamic recrystallization in an Al–Li–Mg–Sc alloy during equal-channel angular extrusion, Mater. Sci. Eng. A 396 (2005) 341–351.
[24] I. Mazurina, T. Sakai, H. Miura, O. Sitdikov, R. Kaibyshev, Grain refinement in aluminum alloy 2219 during ECAP at 250°C, Mater. Sci. Eng. A 473 (2008) 297–305.
[25] I. Mazurina, T. Sakai, H. Miura, O. Sitdikov, R. Kaibyshev, Effect of deformation temperature on microstructure evolution in aluminum alloy 2219 during hot ECAP, Mater. Sci. Eng. A 486 (2008) 662–671.
[26] I. Nikulin, A. Kipelova, S. Malopheyev, R. Kaibyshev, Effect of second phase particles on grain refinement during equal-channel angular pressing of an Al–Mg–Mn alloy, Acta Mater. 60 (2012) 487–497.
[27] A. Mogucheva, E. Babich, B. Ovsyannikov, R. Kaibyshev, Microstructural evolution in a 5024 aluminum alloy processed by ECAP with and without back pressure, Mater. Sci. Eng. A 560 (2013) 178–192.
[28] T. Sakai, A. Belyakov, R. Kaibyshev, H. Miura, J.J. Jonas, Dynamic and post-dynamic recrystallization under hot, cold and severe plastic deformation conditions, Progr. Mater. Sci. 60 (2014) 130–207.
[29] S. Malopheyev, R. Kaibyshev, Strengthening mechanisms in a Zr-modified 5083 alloy deformed to high strains, Mater. Sci. Eng. A 620 (2014) 246–252.
[30] R.Z. Valiev, N.A. Enikeev, M.Y. Murashkin, V.U. Kazykhanov, X. Sauvage, On the origin of the extremely high strength of ultrafine-grained Al alloys produced by severe plastic deformation, Scr. Mater. 63 (2010) 949–952.
[31] S. Malopheyev, V. Kulitskiy, S. Mironov, D. Zhemchuzhnikova, R. Kaibyshev, Friction-stir welding of an Al-Mg-Sc-Zr alloy in as-fabricated and work-hardened conditions, Mater. Sci. Eng. A 600 (2014) 159–170.
[32] X. Sauvage, N. Enikeev, R. Valiev, Y. Nasedkina, M. Murashkin, Atomic-scale analysis of the segregation and precipitation mechanisms in a severely deformed Al–Mg alloy, Acta Mater. 72 (2014) 125–136.
[33] M. Wagenhofer, M. Ann Erickson-Natishan, R.W. Armstrong, F.J. Zerilli, Influences of strain rate and grain size on yield and serrated flow in commercial Al-Mg alloy 5086, Scr. Mater. 41 (1999) 1177–1184.
[34] R.Y. Lapovok, The role of back-pressure in equal channel angular extrusion, J. Mater. Sci. 40 (2005) 341–346.
[35] P.B. Hirsch, A. Howie, R.B. Nicholson, D.W. Pashley, M.J. Whelan, Electron Microscopy of Thin Crystals, second ed., Krieger, New York, 1977.
[36] H. Halim, D.S. Wilkinson, M. Niewczas, The Portevin–Le Chatelier (PLC) effect and shear band formation in an AA5754 alloy, Acta Mater. 55 (2007) 4151–4160.
[37] T.A. Lebedkina, M.A. Lebyodkin, T.T. Lamark, M. Janeček, Y. Estrin, Effect of equal channel angular pressing on the Portevin–Le Chatelier effect in an Al3Mg alloy, Mater. Sci. Eng. A 615 (2014) 7–13.
[38] A. Mogucheva, D. Yuzbekova, R. Kaibyshev, T. Lebedkina, M. Lebyodkin, Effect of grain refinement on Jerky flow in an Al-Mg-Sc alloy, Metall. Mater. Trans. A (2016) 2093–2106.
[39] R. Schwab, V. Ruff, On the nature of the yield point phenomenon, Acta Mater. 61 (2013) 1798–1808.
[40] C.Y. Yu, P.W. Kao, C.P. Chang, Transition of tensile deformation behaviors in ultrafine-grained aluminum, Acta Mater. 53 (2005) 4019–4028.
[41] S.D. Antolovich, R.W. Armstrong, Plastic strain localization in metals: origins and consequences, Prog. Mater. Sci. 59 (2014) 1–160.
[42] M. Zha, Y. Li, R.H. Mathiesen, R. Bjorge, H.J. Roven, Microstructure evolution and mechanical behavior of a binary Al–7Mg alloy processed by equal-channel angular pressing, Acta Mater. 84 (2015) 42–54.
[43] D. Zhemchuzhnikova, R. Kaibyshev, Mechanical behavior of an Al-Mg-Mn-Sc alloy with an ultrafine grain structure at cryogenic temperatures, Adv. Eng. Mater. 17 (2015) 1804–1811.
[44] T. Mukai, K. Higashi, S. Tanimura, Influence of the magnesium concentration on the relationship between fracture mechanism and strain rate in high purity Al-Mg alloys, Mater. Sci. Eng. A 176 (1994) 181–189.
[45] E.L. Huskins, B. Cao, K.T. Ramesh, Strengthening mechanisms in an Al–Mg alloy, Mater. Sci. Eng. A 527 (2010) 1292–1298.
[46] R.W. Cahn, P. Haasen, Physical Metallurgy, fourth ed., North-Holland Physics, Amsterdam, 1996.
[47] Ø. Ryen, O. Nijs, E. Sjolander, B. Holmedal, H.-E. Ekstrom, E. Nes, Strengthening mechanisms in solid solution aluminum alloys, Metall. Mater. Trans. A 37 (2006) 1999–2006.
[48] M.R. Ahmadi, B. Sonderegger, E. Povoden-Karadeniz, A. Falahati, E. Kozeschnik, Precipitate strengthening of non-spherical precipitates extended in <100> or {100} direction in fcc crystals, Mater. Sci. Eng. A 590 (2014) 262–266.
[49] I. Holzer, E. Kozeschnik, Computer simulation of the yield strength evolution in Cu-precipitation strengthened ferritic steel, Mater. Sci. Eng. A 527 (2010) 3546–3551.
[50] M.R. Ahmadi, E. Povoden-Karadeniz, K.I. Oksuz, A. Falahati, E. Kozeschnik, A model for precipitation strengthening in multi-particle systems, Comput. Mater. Sci. 91 (2014) 173–186.

[51] Nh Q. Vo, D.C. Dunand, D.N. Seidman, Atom probe tomographic study of a friction-stir-processed Al–Mg–Sc alloy, Acta Mater. 60 (2012) 7078–7089.
[52] V. Bata, E.V. Pereloma, An alternative physical explanation of the Hall–Petch relation, Acta Mater. 52 (2004) 657–665.
[53] N. Hansen, Hall–Petch relation and boundary strengthening, Scr. Mater. 51 (2004) 801–806.
[54] Z. Yanushkevich, A. Mogucheva, M. Tikhonova, A. Belyakov, R. Kaibyshev, Structural strengthening of an austenitic stainless steel subjected to warm-to-hot working, Mater. Charact. 62 (2011) 432–437.
[55] X. Zhang, A. Godfrey, X. Huang, N. Hansen, Q. Liu, Microstructure and strengthening mechanisms in cold-drawn pearlitic steel wire, Acta Mater. 59 (2011) 3422–3430.
[56] P. Kusakin, A. Belyakov, Ch Haase, R. Kaibyshev, D.A. Molodov, Microstructure evolution and strengthening mechanisms of Fe-23Mn-0.3C-1.5Al TWIP steel during cold rolling, Mater. Sci. Eng. A 617 (2014) 52–60.
[57] V. Kulitskiy, S. Malopheyev, S. Mironov, R. Kaibyshev, Grain refinement in an Al-Mg-Sc alloy: equal channel angular pressing versus friction-stir processing, Mater. Sci. Eng. A 674 (2016) 480–490.
[58] R. Mishnev, I. Shakhova, A. Belyakov, R. Kaibyshev, Deformation microstructures, strengthening mechanisms, and electrical conductivity in a Cu–Cr–Zr alloy, Mater. Sci. Eng. A 629 (2015) 29–40.
[59] S. Takaki, D. Akama, N. Nakada, T. Tsuchiyama, Effect of grain boundary segregation of interstitial elements on Hall-Petch coefficient in steels, Mater. Trans. 55 (2014) 28–34.
[60] T.C. Schulthess, P.E.A. Turchi, A. Gonis, T.G. Nieh, Systematic study of stacking fault energies of random Al-based alloys, Acta Mater. 46 (1998) 2215–2221.
[61] S. Lu, Q.-M. Hub, B. Johansson, L. Vitos, Stacking fault energies of Mn, Co and Nb alloyed austenitic stainless steels, Acta Mater 59 (2011) 5728–5734.
[62] D.J. Lloyd, S.A. Court, Influence of grain size on tensile properties of Al-Mg alloys, Mater. Sci. Technol. 19 (2003) 1349–1354.
[63] H. Hasegawa, S. Komura, A. Utsunomiya, Z. Horita, M. Furukawa, M. Nemoto, T.G. Langdon, Thermal stability of ultrafine-grained aluminum in the presence of Mg and Zr additions, Mater. Sci. Eng. A 265 (1999) 188–196.
[64] T.H. Courtney, Mech. Behav. Mater. (2000) 1–210. Waveland, Illinois.
[65] N. Balasubramanian, T.G. Langdon, The strength–grain size relationship in ultrafine-grained metals, Metall. Mater. Trans. A (2016) 5827–5838.
[66] J. Kang, R.K. Mishra, D.S. Wilkinson, O.S. Hopperstad, Effect of Mg content on Portevin–Le Chatelier band strain in Al–Mg sheet alloys, Phil. Mag. Let. 92 (2012) 647–655.